

PAPER

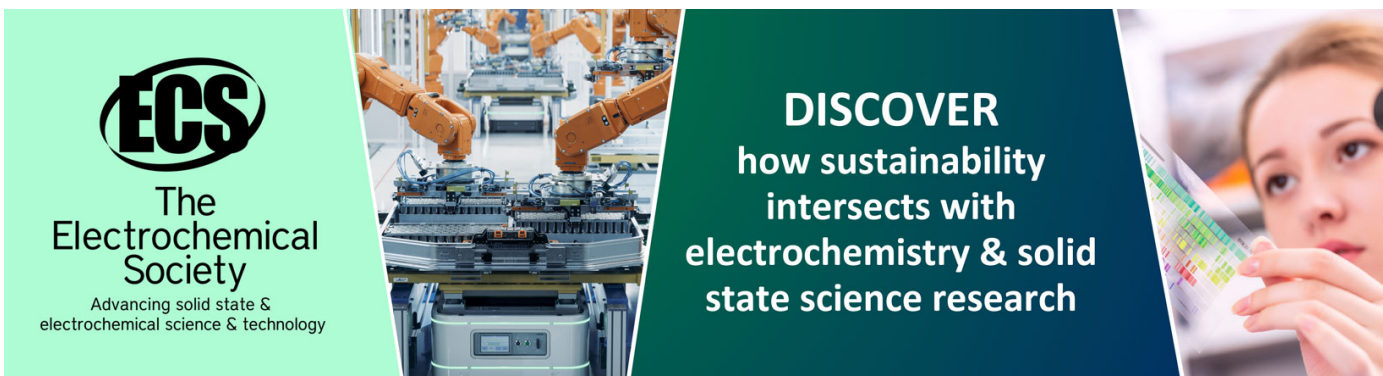
Fabrication of hollow boron-doped diamond nanostructure via electrochemical corrosion of a tungsten oxide template

To cite this article: Young-Kyun Lim *et al* 2018 *Nanotechnology* **29** 325602

View the [article online](#) for updates and enhancements.

You may also like

- [Electrochemical Recovery of Copper from Model Wastewater Using Boron-Doped Diamond Electrodes](#)
Keisuke Natsui, Chizu Yamaguchi and Yasuaki Einaga
- [Electroreduction of CO₂ into CO Using Amine-Modified Diamond Electrode](#)
Takashi Yamamoto, Tatsuhiko Mikami, Mai Tomisaki *et al.*
- [Flexible Boron-Doped Diamond Films for Bio-Potential Sensing in Plants](#)
Shoko Tago, Tsuyoshi Ochiai, Mio Hayashi *et al.*



ECS
The
Electrochemical
Society
Advancing solid state &
electrochemical science & technology

DISCOVER
how sustainability
intersects with
electrochemistry & solid
state science research

Fabrication of hollow boron-doped diamond nanostructure via electrochemical corrosion of a tungsten oxide template

Young-Kyun Lim, Eung-Seok Lee, Choong-Hyun Lee and Dae-Soon Lim 

Department of Materials Science and Engineering, Korea University, Seoul 02841, Republic of Korea

E-mail: dslim@korea.ac.kr

Received 2 February 2018, revised 11 May 2018

Accepted for publication 22 May 2018

Published 7 June 2018



Abstract

In the study, a hollow boron-doped diamond (BDD) nanostructure electrode is fabricated to increase the reactive surface area for electrochemical applications. Tungsten oxide nanorods are deposited on the silicon substrate as a template by the hot filament chemical vapor deposition (HFCVD) method. The template is coated with a 100 nm BDD layer deposited by HFCVD to form a core-shell nanostructure. The WO_x core is finally electrochemically dissolved to form hollow BDD nanostructure. The fabricated hollow BDD nanostructure electrode is investigated via scanning electron microscopy, transmission electron microscopy, and Raman spectroscopy. The specific surface areas of the electrodes were analyzed and compared by using Brunauer–Emmett–Teller method. Furthermore, cyclic voltammetry and chronocoulometry are used to investigate the electrochemical characteristics and the reactive surface area of the as-prepared hollow BDD nanostructure electrode. A hollow BDD nanostructure electrode exhibits a reactive area that is 15 times that of a planar BDD thin electrode.

Keywords: hollow structure, boron-doped diamond, electrochemical corrosion, tungsten oxide, reactive surface area

(Some figures may appear in colour only in the online journal)

1. Introduction

Nanocrystalline boron-doped diamond (BDD) is an attractive electrode candidate for electrochemical applications due to its unique physical and chemical stabilities as well as its remarkable electrochemical characteristics including a low, stable background current, wide potential window, and good biocompatibility [1–3]. In order to achieve superior performance for electrochemical applications, nanostructured BDD is developed and exhibits a high specific surface area per the geometrical surface area of the electrode, and this enhances the reactive surface area and the electron transfer kinetics [4]. The development of nanostructured materials is important in various fields because the materials allow for device performance improvements that are impractical while using micro or bulk-size materials [5]. The surface-to-volume ratio effect of nanostructured materials provides performance enhancements in devices with electrochemical applications, such as chemical

and bio-sensors [6, 7], batteries [8], supercapacitors [9–12] and wastewater treatment [13].

Various methods are developed to fabricate nanostructured BDD electrodes with larger active surface areas. It provides additional sites where the electrochemical reaction occurs. A boron-doped diamond nanorod forest electrode was manufactured by synthesizing diamond on a silicon nanowire, and the electrode exhibited an enhanced sensitivity for glucose detection when compared to that of a planar BDD electrode [14]. Wang *et al* adjusted the length of the BDD nanowires in the electrode via a maskless reactive ion etching process with oxygen plasma and reported an improvement in the glucose detection performance [15]. A nano-porous BDD film with a honeycomb structure was fabricated by etching polished polycrystalline diamond films through porous alumina masks with an oxygen plasma, and the structure allowed the storage of additional charge per unit capacitance [16].

In order to further improve the performance of an electrode, hollow nanostructures with various shapes such as a sphere, fiber, or box, are developed and exhibit increased surface areas and lower densities than that of existing nanostructured materials [17]. The most common method to fabricate a hollow structure involves removing the templates covered with functional materials via calcination by thermal treatment, chemical etching, or the Kirkendall effect [18–23]. For example, Kondo *et al* developed a BDD hollow fiber membrane by chemically etching a quartz filter substrate consisting of quartz fibers [23]. Unfortunately, in most cases, treatments with hazardous chemicals, such as HF, or energy consumption and expensive equipment for calcination at a high temperature are required to eliminate the template. Although hollow structures are actively developed by using a variety of functional materials, there is a paucity of studies on a hollow structure composed of diamond or BDD materials.

In this study, we developed a hollow BDD nanostructure electrode by the electrochemical corrosion of a tungsten oxide nanorod support material surrounded by BDD without expensive equipment, harmful chemicals, or a complicated process. Tungsten can be electrochemically corroded at an appropriate voltage applied in an ionic liquid electrolyte, and thus tungsten oxide was selected as a template [24, 25]. The BDD film was synthesized on a template of tungsten oxide nanorods, and only BDD nanostructures remained and retained their structure after the tungsten oxides were dissolved to the electrolyte via corrosion. The structure offered reactive sites for target components on both the outer and inner sides of the BDD nanorod. Hence, the hollow BDD nanostructure electrode exhibited a better electrochemical performance when compared with that of solid BDD nanorods with identical morphology. The electrostatic self-assembly of nanodiamond (ESAND) process was adopted to attach the nanodiamond particles as nuclei for the deposition of the BDD films on a tungsten oxide nanostructured template [26]. By using the ESAND process, the nanocrystalline diamond film was deposited on the nanoscale substrate with minimal damage [27]. In order to investigate the improved properties and increased reactive surface area of the hollow BDD nanostructure electrode were analyzed by using a cyclic voltammetry (CV) and a chronocoulometry (CC) methods compared to those of the planar BDD electrode. The increment of the electrochemical reactive surface area was compared to that of specific surface area calculated by Brunauer–Emmett–Teller (BET) method.

2. Experimental

2.1. Preparation of the WO_x nanorods on a Si substrate

Tungsten oxide nanorods were prepared by a thermal evaporation process in a chemical vapor deposition (figure 1(a)). An array of tungsten wires ($d = 0.5$ mm, 99.5%) was placed 5 mm above the (100)-oriented silicon substrate (20 mm \times 20 mm) as the tungsten precursor. After evacuating the chamber to less than

4.0×10^{-3} Torr, the temperature of the substrate increased to 850 °C at a rate of 20 °C min⁻¹. When the temperature reached 850 °C, the heater of the substrate was turned off, and the tungsten filaments were subsequently heated to a temperature of 1700 °C by applying an AC voltage for 10 min. After deposition, the chamber was cooled down to room temperature.

2.2. Synthesis of nanocrystalline BDD

In order to synthesize BDD on the tungsten oxide nanorods, nanodiamond particles that acted as nuclei for diamond growth should be attached to the surface of the tungsten oxide nanorods by using the ESAND technique [26] (figure 1(b)). An anionic poly (sodium 4-styrenesulfonate) coated nanodiamond solution was prepared by using attrition milling, and the solution is called the PSS-ND solution. In order to attach the nanodiamond particles to the tungsten oxide nanorods, the as-synthesized samples were immersed into the PSS-ND solution for 4 h. Subsequently, the samples were softly rinsed by D.I water and dried with N₂ gas blowing.

The BDD film was synthesized by HFCVD with 1% CH₄, 0.05% B₂H₆, and 98.95% H₂ for 8 h. The total flow rate of the gas mixture was 100 sccm and the working pressure was 70 Torr (figure 1(c)). The temperatures of the substrate and the filament were maintained at 800 °C and 1900 °C, respectively, during the deposition.

2.3. Fabrication of the hollow BDD nanostructure

As shown in figure 2, a constant potential (1 V versus Ag/AgCl sat KCl) was applied for the corrosion of the tungsten oxide nanorods that were placed inside the BDD nanorods, by using a three-electrode cell in an acetate buffer solution (pH 4.8) for 2 h. An Ag/AgCl electrode and Pt coil were used as the reference and counter electrodes, respectively. The tungsten oxide nanorods that were surrounded by BDD, oxidized to tungstate ions through the structural openings when the reaction voltage was applied. Thus, hollow BDD nanostructure was fabricated as shown in figure 1(d).

2.4. Characterization

The morphology and structure of the synthesized tungsten oxide and BDD films were inspected by using field emission scanning electron microscopy (FESEM, Hitachi S-4300), x-ray diffractometry (XRD, Rigaku SmartLab) and Raman spectroscopy (HORIBA JOBIN YVON LabRam ARAMIS IR2, 532 nm diode laser). Transmission electron microscopy (TEM, TitanTM 80-300) analysis and high resolution-TEM (HRTEM, TitanTM 80-300) analysis with a selective area electron diffraction pattern acquisition apparatus were carried out to investigate the structure of the WO_x /BDD and hollow structure BDD nanotube. In order to verify that the tungsten was removed from the inside the BDD nanorods during the oxidation process, TEM (Tecnai F20 G2) analysis equipped with an energy-dispersive x-ray spectrometer (EDS) was performed. Furthermore, the amount of tungsten in the acetate

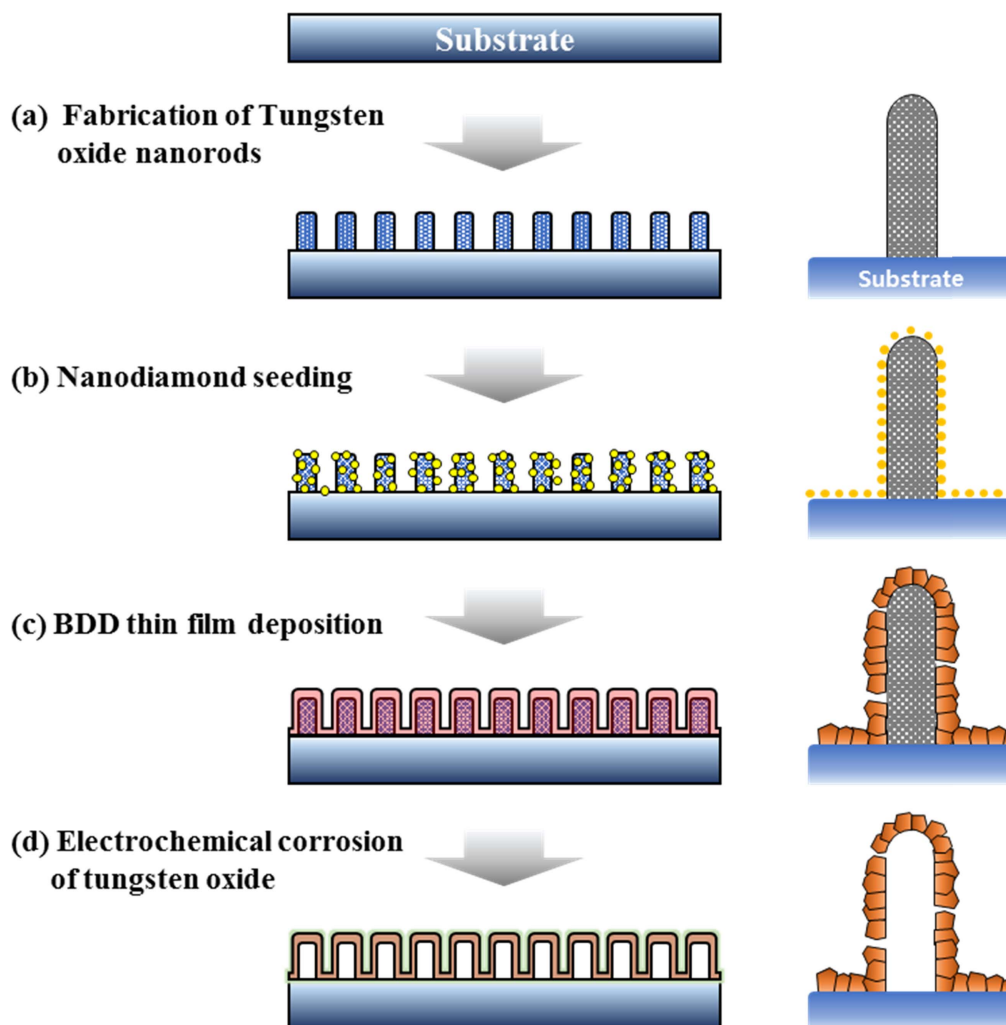


Figure 1. Schematic diagram of the fabrication process of the hollow BDD nanostructure and illustrations of a nanorod produced by each step. (a) Tungsten oxide nanorods are deposited on the substrate by CVD. (b) Nanodiamond particles are attached to the surface of the tungsten oxide nanorods. (c) BDD thin film is deposited on the tungsten oxide nanorods by HFCVD. (d) Tungsten oxide nanorods are eliminated by electrochemical corrosion.

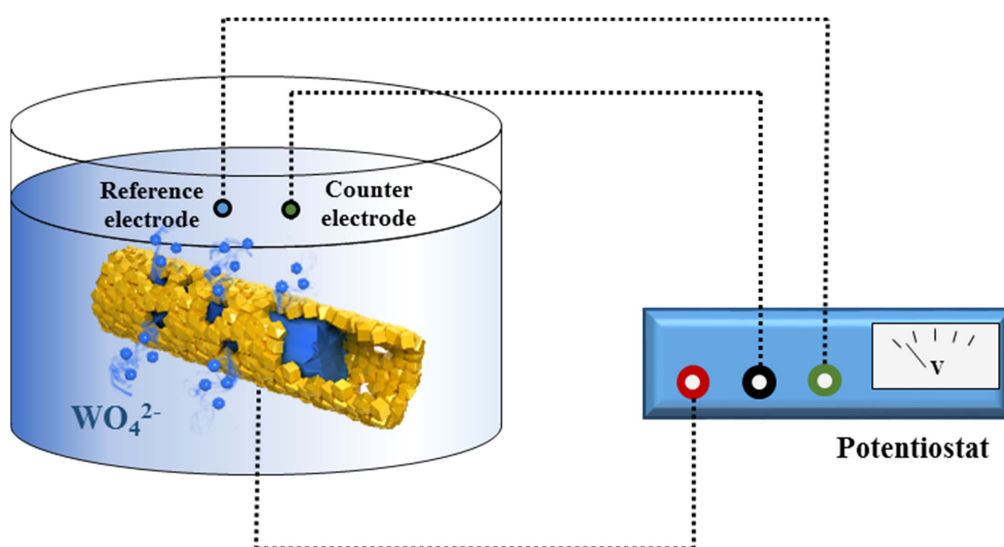


Figure 2. Schematic diagram and illustration of the method for electrochemical corrosion of tungsten oxides to acquire hollow BDD nanostructure.

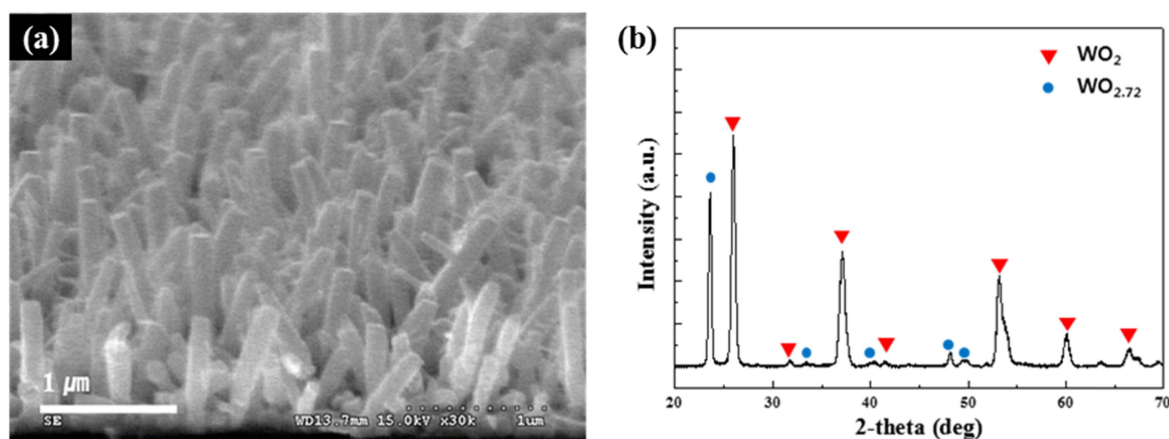


Figure 3. (a) SEM image and (b) XRD pattern of the as-synthesized tungsten oxide nanorods.

buffer solution was analyzed by using an inductively coupled plasma atomic emission spectrophotometer (ICP-AES, Jobin Yvon Ultima2).

The electrochemical properties were examined by CV and CC by using a potentiostat instrument (Princeton Applied Research, VersaSTAT3) connected to a three-electrode cell consisting of platinum (Pt) coil as the counter electrode, an Ag/AgCl reference electrode, and modified BDD electrodes (a planar BDD and hollow BDD nanostructure).

The BET method with krypton as the adsorption gas was performed at 77 K (ASAP 2020 Micromeritics). The samples were degassed under vacuum at 150 °C for 9 h prior to measurement. The krypton adsorption isotherms were collected at 77 K under the relative pressure (P/P_0) range of 0.04–0.5. The specific surface area was calculated from the BET plot in the relative pressure range of 0.17–0.31 except for the nonlinear range.

3. Results and discussion

The surface morphology of the as-synthesized tungsten oxide nanorod sample was investigated by FESEM (figure 3(a)). The heating of the tungsten filament to 1700 °C resulted in a tungsten oxide nanostructure with a length of 0.8–1.0 μm and approximately 100 nm diameter nanorods on the as-annealed silicon substrate. The synthesis mechanism of the tungsten oxides can be described by using the vapor–solid growth mechanism. The vaporized W or WO_x ($x = 2–3$) from the tungsten filaments attached to the silicon substrate, and the supersaturated tungsten oxides subsequently tended to form solid tungsten oxide clusters. The clusters acted as seeds for growth and favorably absorbed tungsten species. A one-dimensional (1D) nanostructure can be grown based on the crystallinity of the seed [28].

The XRD pattern of the as-grown tungsten oxide nanorods indicated that the nanorods contained WO₂ (JCPDS No: 32-1393) and WO_{2.72} (JCPDS No: 73-2177) (figure 3(b)). Although an external flow of oxygen was not provided, oxygen could be obtained from the air that leaked into the chamber, and thus tungsten oxide was created instead of tungsten. It was difficult to

clearly identify the stoichiometry of tungsten oxide by using the XRD pattern because tungsten oxide compounds exhibit similar crystal structures [29]. The as-synthesized tungsten oxide nanorods can contain WO₂, WO_{2.72}, and other non-stoichiometric tungsten oxides (WO_x, $x = 2–3$).

The ESAND process was used to cover the tungsten nanorods with nanodiamond particles that acted as seeds for the nanocrystalline BDD film deposition, and core–shell structure WO_x/BDD nanorods were subsequently fabricated by the HFCVD deposition (figures 4(a), (b)). As shown in figures 4(a) and (b), the tungsten oxide nanorods were clearly identified that the nanorods are surrounded with BDD film successfully. Owing to the well-dispersed nanodiamond particles from ESAND process, we obtained core/shell nanorods composed of tungsten oxide and BDD with a uniform diameter of approximately 250 nm. As shown in figure 4(c) the dark areas that are evidently observed in figures 4(a) and (b) were not detected after oxidation of tungsten oxide, thereby implying that most of the tungsten oxides vanished from the inside the BDD nanorods. The density of the nanorods slightly decreased because a few nanorods with a sparse number of attached diamond clusters could not sustain its structure after the tungsten oxide template was removed, although most of the nanorods remained and were densely covered with diamond clusters.

The TEM analysis provides additional information about the structural features of the as-prepared samples (figures 5(a)–(d)). The TEM image of the WO_x/BDD sample indicates that the diamond clusters covered the 1D tungsten oxide nanorods and formed a layer with a thickness of 100 nm (figure 5(a)). The HRTEM image of the WO_x/BDD (figure 5(b)), the investigated area is denoted by the white square in figure 5(a) verified that the cluster is a diamond structure with a lattice spacing of 0.205 nm, and this corresponded to the (111) planes of a cubic diamond. Dark area shows that monoclinic (220) WO₃ phase with the lattice spacing 0.268 nm.

After electrochemical corrosion test, nanostructure is only composed of diamond crystalline (figures 5(c) and (d)). The selected area electron diffraction (SAED) pattern (the inset of figure 5(d)) also confirmed that the cluster was a

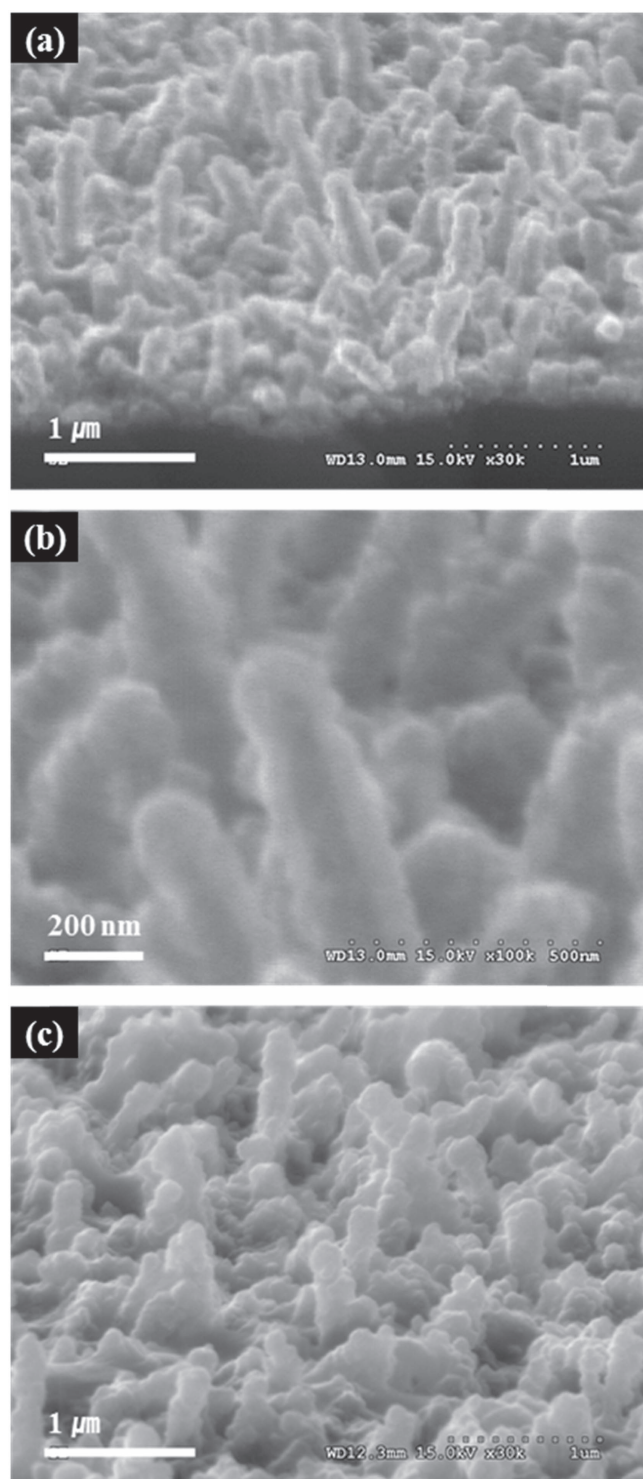


Figure 4. SEM image of (a), (b) tungsten oxide nanorods surrounded with BDD (WO_x/BDD) and (c) hollow BDD nanostructure.

diamond structure (JCPDS No: 6-675). The results of EDS confirm that core tungsten material is completely removed after electrochemical treatment (figures 5(e) and (f)).

Raman spectroscopy was used to analyze the structural phases of WO_x/BDD and hollow BDD nanostructure. The spectrum show that WO_x nanorods composed of several types of tungsten oxides such as $\text{WO}_{2.72}$ and WO_3 (figure 6(a)). The

band at 129 cm^{-1} was related to the W–O–W bending modes, and the band at 263 cm^{-1} was related to the O–W–O bending modes. The two peaks at 708 and 805 cm^{-1} were related to the W–O stretching vibrations [30]. A shoulder peak at 940 cm^{-1} was speculated to originate from the W=O stretching mode of the terminal oxygen on the surface of the samples [31].

After the BDD deposition on the outer side of the tungsten oxide nanorods, two discrete and broad peaks appeared at 1340 and 1590 cm^{-1} , and this corresponded to the typical graphitic D-band and G-band that originated in the BDD, respectively (figure 6(b)). When compared to the spectrum of the as-synthesized tungsten oxide sample, the peaks at 708 and 805 cm^{-1} were clearer in figure 6(b), and this indicated that the amount of crystalline tungsten oxide increased via the heat treatment during the BDD deposition in the HFCVD system [32]. The two peaks at 185 and 237 cm^{-1} were separate from a broad peak at 263 cm^{-1} of WO_x , and an increased peak at 129 cm^{-1} suggested that the tungsten oxide transitioned from amorphous to the crystalline structure via the heat treatment at the BDD deposition temperature of approximately 800°C [33].

The tungsten-related peaks decreased significantly and the carbon-related peaks at 1340 and 1590 cm^{-1} predominantly increased after the oxidation of tungsten components to tungstate ions (figure 6(c)). The disappearance of peaks at approximately 260 , 700 and 805 cm^{-1} indicated that only a few tungsten components existed inside the BDD nanostructure, and the site in which the tungsten oxide existed became empty space. The result revealed that the remaining nanostructures were mainly constructed by BDD with a hollow structure.

The Raman spectrum of the planar BDD thin film that was used as a comparison target and fabricated by using HFCVD under the same BDD deposition conditions for WO_x/BDD exhibited peaks at 1150 , 1340 , 1480 , and 1560 cm^{-1} (figure 6(d)). A comparison of the spectrum of the planar BDD indicated that the spectrum of the hollow structure was similar to that of the planar BDD. Hence, peaks at 1150 and 1480 cm^{-1} were also detected in that of the hollow BDD nanostructure. The peaks originated from trans-polyacetylene content in the grain boundaries of the nanocrystalline diamond film [34, 35].

However, the peak of the sp^3 diamond phase at 1332 cm^{-1} was not clear because boron doping interrupts the diamond lattice [36]. In addition, a small nanocrystalline diamond grain size resulted in the existence of a high amount of non-diamond carbon in the grain boundary, and it potentially affected the peak of the sp^3 diamond phase at 1332 cm^{-1} [37]. The G-band related peak at 1560 cm^{-1} shifted to 1590 cm^{-1} compared to that for the planar BDD due to the increase in the non-diamond phase in the grain boundaries that was caused by the smaller size of the diamond clusters compared to those in the planar BDD [38]. The sharp band in the spectrum at 520 cm^{-1} that was also observed for the planar BDD and corresponded to the silicon substrate.

Consequently, the hollow BDD nanostructure sample exhibited D- and G- bands and slight peaks at 1140 and

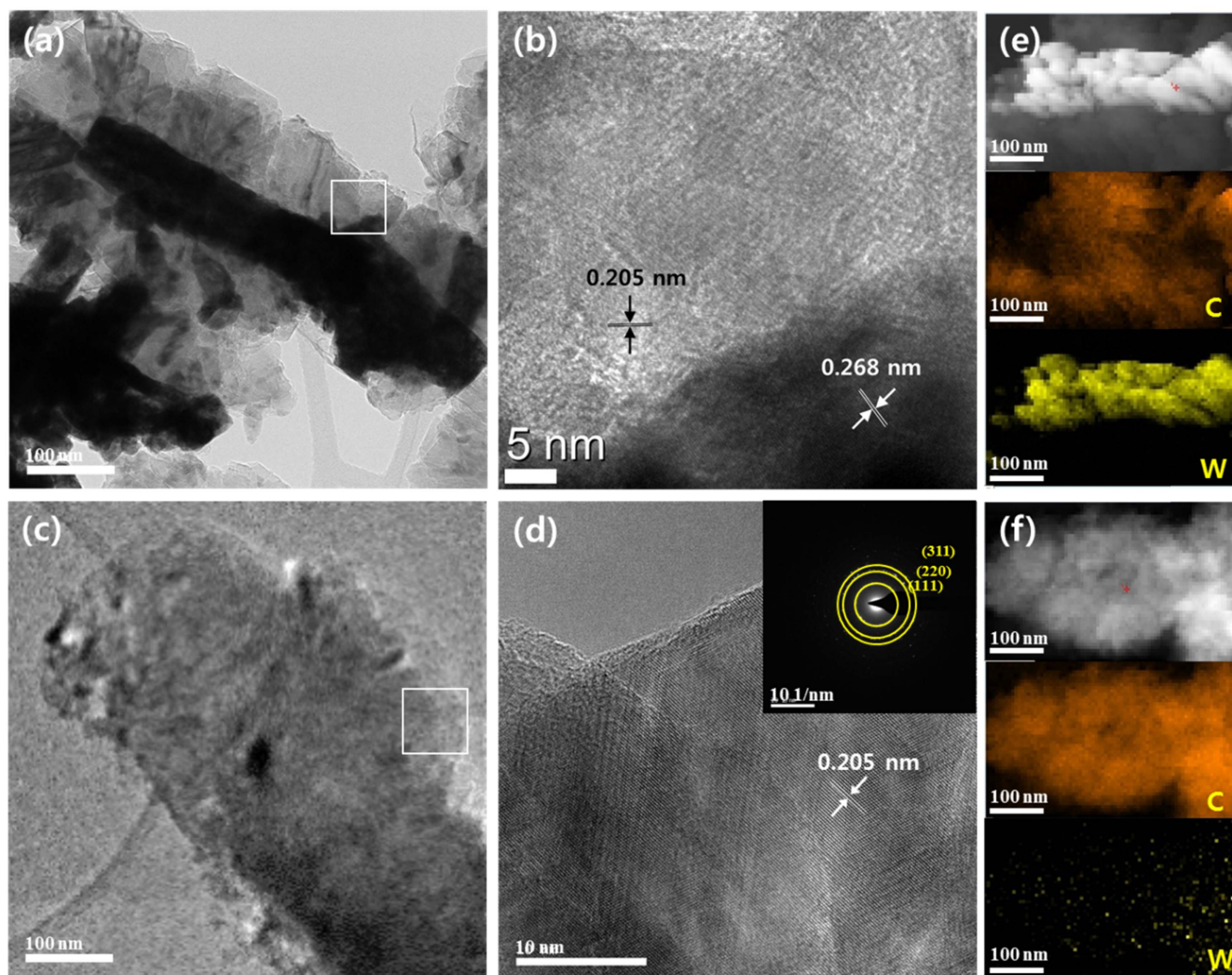


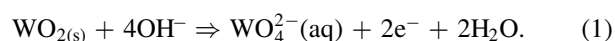
Figure 5. TEM and HRTEM images of (a), (b) WO_x/BDD and (c), (d) hollow BDD nanostructure (inset: SAED pattern of a hollow BDD nanostructure). Annular dark field images and EDS mapping for C and W elements of the (e) WO_x/BDD and (f) hollow BDD nanostructure.

1480 cm^{-1} indicated that the nanocrystalline diamond phase was well deposited on the as-synthesized tungsten oxide sample in terms of Raman spectrum, and it coincided with the result of the SAED pattern of the hollow BDD nanostructure.

Specifically, ICP-AES was used to determine whether the tungsten in the WO_x/BDD sample dissolved into the acetate buffer electrolyte during the oxidation process (figure 7). The amounts of tungsten that were oxidized from the WO_x/BDD sample when a voltage was applied were analyzed by ICP-AES at two pH values, namely 3.2 and 4.8. As shown in figure 7, the dissolved tungsten concentration in the solution linearly increased with the oxidation time at pH 4.8 while dissolved tungsten was rarely detected in solution for 10 min at pH 3.2. The results indicated that the tungsten components inside the BDD nanorods were readily oxidized into tungstate ions and dissolved in the solution at pH 4.8, and thus hollow BDD nanostructure were obtained.

Based on the Pourbaix diagram of tungsten, at a pH above 4.5, solid tungsten components can be transformed into tungstate ions, such as WO_4^{2-} , instead of tungsten oxides in a solid phase, namely, WO_2 , W_2O_5 , and WO_3 , when a sufficient

voltage is applied [39]. The reaction mechanism for the anodic dissolution of tungsten oxide was described by Kelsey [40] as follows:



As shown in equation (1), at a higher pH value, a sufficient concentration of OH^- in the electrolyte promotes the reaction of anodic oxidation of the tungsten components, and WO_4^{2-} is the expected product of the tungsten oxide dissolution [41]. Similarly, non-stoichiometric tungsten oxide (WO_x , $2 < x < 3$) such as $\text{WO}_{2.72}$ was oxidized to WO_3 , that dissolved as WO_4^{2-} in the presence of OH^- ions [42].

Additionally, CV was performed to further investigate the change in the WO_x/BDD electrodes as the tungsten oxide template oxidizes and the electrochemical properties of the as-prepared electrodes in a 3 M KCl solution containing 10 mM $\text{K}_3[\text{Fe}(\text{CN})_6]$ at a scan rate of 10 mV s^{-1} with an applied voltage ranging from -1 to 1 V (versus Ag/AgCl) (figure 8).

As shown in figure 8(a), the CV of the as-prepared WO_x substrate indicates electrochemical behavior similar to that of non-stoichiometric tungsten, and the oxidation peak was located

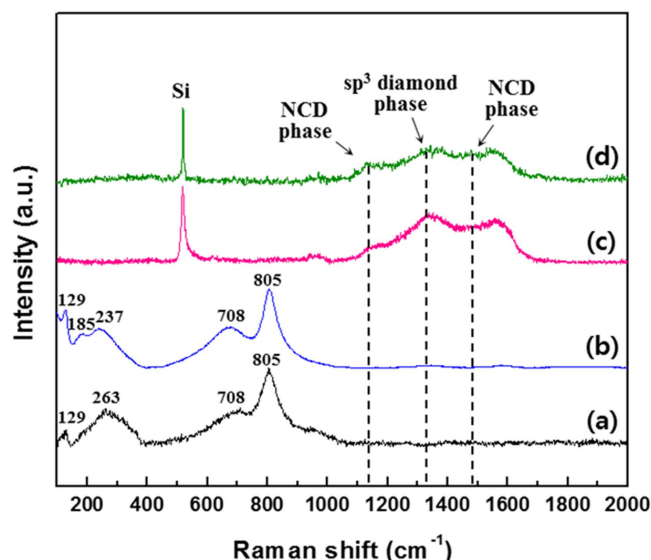


Figure 6. Comparison of the Raman spectra from 100 to 2000 cm^{-1} for the as-prepared samples: (a) WO_x , (b) WO_x/BDD , (c) hollow BDD nanostructure, and (d) planar BDD.

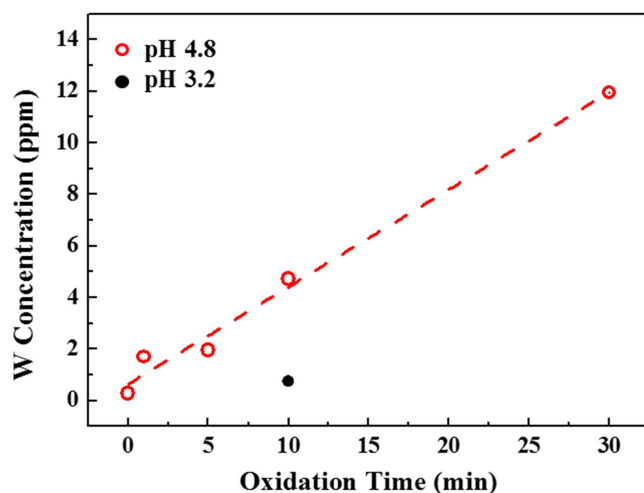


Figure 7. Variation in tungsten concentration measured with ICP-AES as a function of oxidation time in the electrolyte from the WO_x/BDD sample at two pH values, namely 3.2 and 4.8.

at 0.49 V [43]. The CV for the WO_x/BDD electrode (in which a few tungsten oxides remained due to the insufficient oxidation time for the tungsten components) revealed two oxidation peaks at 0.39 V and 0.77 V. Compared to the typical CV of a BDD electrode [44], the second peak at 0.77 V was affected by the reaction at the surface of the tungsten oxide residues that were not oxidized out of the BDD nanorods. However, with respect to the hollow BDD structure electrode, the tungsten components were oxidized for a sufficient amount of time corresponding to approximately 120 min, and the peak affected by tungsten oxide disappeared. The result indicated that the tungsten oxide completely moved from the BDD nanorods and that the BDD nanorods exhibited voids in which the tungsten oxides existed.

As shown in figure 8(b), the anodic peak current ($I_{p,a}$) of the hollow BDD nanostructure (1.37 mA) electrode increased approximately 6 times compared to that of the planar BDD

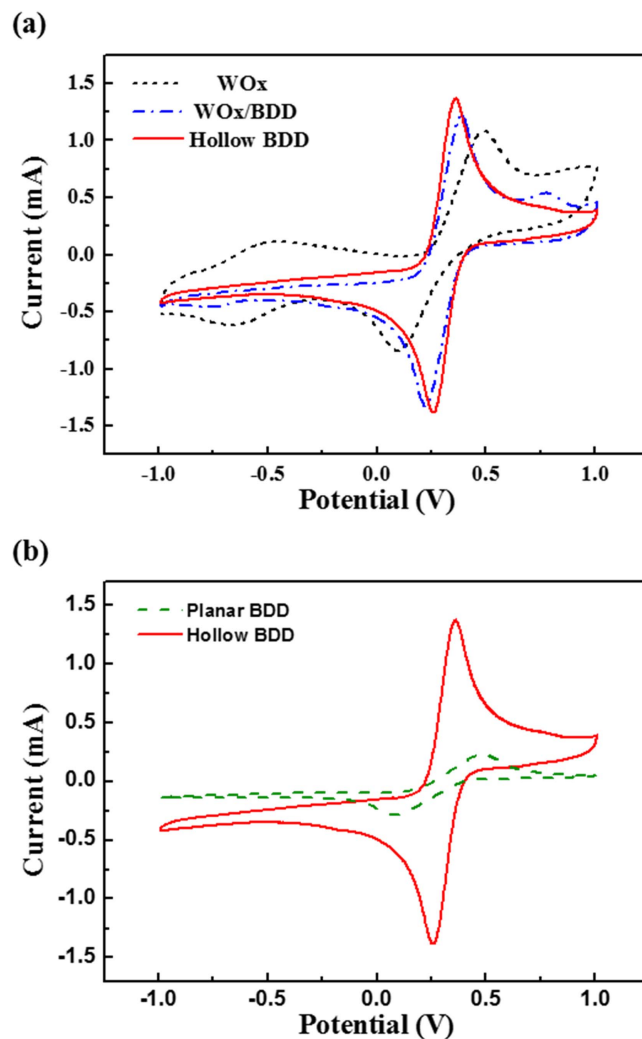


Figure 8. Cyclic voltammograms of (a) tungsten oxides: WO_x (black), WO_x/BDD (blue) and hollow BDD nanostructure (red) electrodes; (b) planar BDD (green) and hollow BDD nanostructure (red) in a 3 M KCl solution containing 10 mM $\text{K}_3[\text{Fe}(\text{CN})_6]$ at a scan rate of 10 mV s^{-1} .

electrode (0.23 mA) due to the increase in the reactive surface area that resulted from the hollow structure [45]. Furthermore, the peak-to-peak separation potential (ΔE_p) value of the hollow BDD nanostructure (0.10 V) was significantly reduced compared to that of the planar BDD (0.41 V). This indicated that the charge transfer kinetics of hollow BDD nanostructure electrode is superior to that of the planar BDD [46].

The CC technique was performed to investigate the real electrochemical reactive surface areas of the as-fabricated electrodes in a 0.1 M KCl solution containing 0.1 mM $\text{K}_3[\text{Fe}(\text{CN})_6]$. The charge produced by the redox reaction at the electrode is given by the Anson equation as follows: [47]

$$Q = 2nFACD^{1/2}t^{1/2}\pi^{-1/2} + Q_{dl} + Q_{ads}, \quad (2)$$

where Q denotes the charge (C), n represents the number of electrons transferred, F denotes Faraday's constant (96485 C mol^{-1}), A (cm^2) denotes the electrochemical reactive surface area, C (mol cm^{-3}) denotes the concentration of the oxidized species, D ($\text{cm}^2 \text{ s}^{-1}$) denotes the diffusion coefficient, t (s) denotes the time, Q_{dl} denotes the double-layer charge, and

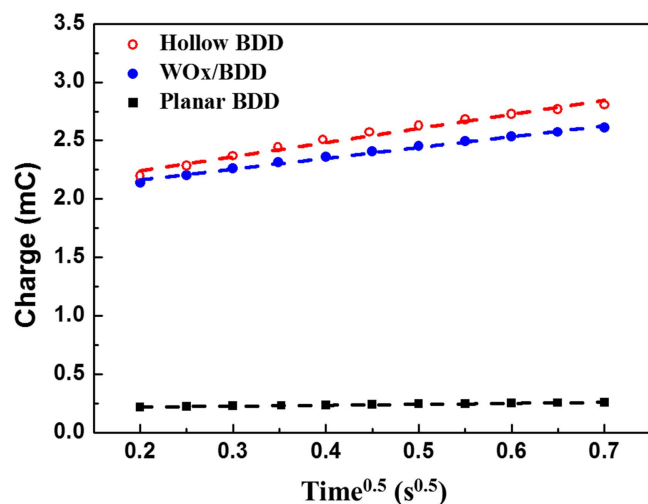


Figure 9. Chronocoulometric charge (Q) versus $(\text{time})^{1/2}$ plots of planar BDD, WO_x/BDD and hollow BDD nanostructure electrodes in a 0.1 M KCl solution containing 0.1 mM $\text{K}_3[\text{Fe}(\text{CN})_6]$.

Table 1. Comparison of reactive surface areas and BET surface areas of the planar BDD, WO_x/BDD and hollow BDD nanostructure.

Electrode	Reactive surface area (cm^2)	BET surface area ($\text{cm}^2 \text{g}^{-1}$)
Planar BDD	2.57 ± 0.25	—
WO_x/BDD	24.72 ± 7.12	88.50 ± 13.37
Hollow BDD	39.14 ± 1.18	146.83 ± 4.23

Q_{ads} denotes the faradic component due to the oxidation of adsorbed species. The electrochemical reactive surface area (A) of the electrodes was calculated by using the slope of the plot of Q versus $t^{1/2}$. In this study, the diffusion coefficient (D) of 0.1 mM $\text{K}_3[\text{Fe}(\text{CN})_6]$ was $7.6 \times 10^{-6} \text{ cm}^2 \text{ s}^{-1}$ [48] and $n = 1$.

Figure 9 shows the $Q-t^{1/2}$ curve from the CC response. By using Anson plot and the Anson equation (equation (2)) introduced previously, the average reactive surface area estimated and shown in table 1. Hollow BDD nanostructure shows the largest reactive surface area of 39.14 cm^2 .

The specific surface area of WO_x/BDD and hollow BDD nanostructure were characterized by the Kr adsorption process at 77 K. The BET adsorption plots are shown in figure 10. Table 1 shows a comparison of the BET average surface area calculated for WO_x/BDD and hollow BDD nanostructure. The hollow BDD nanostructure present larger specific surface area of $146.83 \text{ cm}^2 \text{ g}^{-1}$ compared with that of WO_x/BDD nanostructure. These results indicated that the increments of electrochemical reactive surface area and BET surface area seem reasonable when we consider additional inner surface of hollow nanostructures. The average values of reactive surface area and BET surface area were summarized in table 1.

4. Conclusions

In this study, a hollow BDD nanostructure electrode was efficiently fabricated by electrochemical corrosion of the tungsten

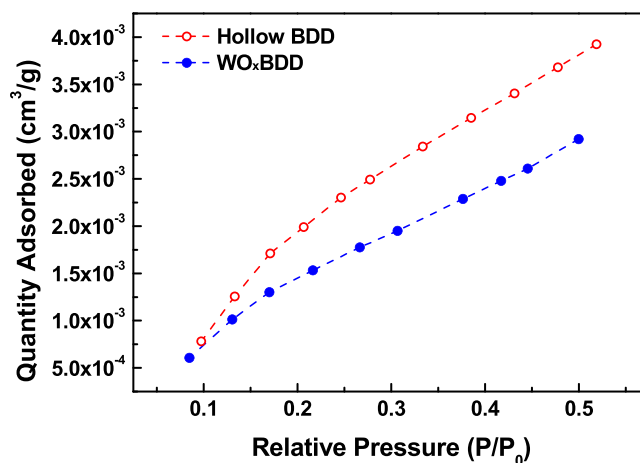


Figure 10. Kr adsorption isotherm for WO_x/BDD and hollow BDD nanostructure at 77 K.

oxide nanorods surrounded by nanocrystalline BDD. Tungsten oxides, such as WO_2 , $\text{WO}_{2.72}$, and WO_3 , were oxidized to tungstate ions (WO_4^{2-}) in an acetate buffer solution (pH 4.8) under sufficient voltage. The tungsten components were successfully removed from the WO_x/BDD nanorods, and the hollow BDD nanostructure maintained the morphology of the nanorods and provided an additional reactive site inside of the BDD nanorods. The hollow structure possessed a larger reactive surface area and improved electrochemical properties compared to that of a planar BDD electrode. Moreover, the reactive surface area of the hollow BDD nanostructure exhibited 1.6 times that of WO_x/BDD . It indicated that the generation of hollow space inside of the BDD nanorods is helpful to increase the reactive surface area and enhance the electrochemical performance of the electrode. In conclusion, this study proposes a simple, harmless, and controllable fabrication method for a hollow BDD nanostructure.

Acknowledgments

This study was supported by the Korea Ministry of Environment (MOE) as ‘Public Technology Program based on Environmental Policy’ (No. E416-00070-0604-0).

ORCID iDs

Dae-Soon Lim  <https://orcid.org/0000-0003-0165-7656>

References

- [1] Pleskov Y V, Sakharova A Y, Krotova M D, Bouilov L L and Spitsyn B V 1987 *J. Electroanal. Chem.* **228** 19–27
- [2] Swain G M, Anderson A B and Angus J C 1998 *MRS Bull.* **23** 56–60
- [3] Swain G M and Ramesham R 1993 *Anal. Chem.* **65** 345–51
- [4] Yang N J, Foord J S and Jiang X 2016 *Carbon* **99** 90–110
- [5] Guo Y G, Hu J S and Wan L J 2008 *Adv. Mater.* **20** 2878–87

- [6] Kong J, Franklin N R, Zhou C W, Chapline M G, Peng S, Cho K J and Dai H J 2000 *Science* **287** 622–5
- [7] Song M J, Lee S K, Kim J H and Lim D S 2013 *J. Electrochem. Soc.* **160** B43–6
- [8] Jiang J A, Li Y Y, Liu J P and Huang X T 2011 *Nanoscale* **3** 45–58
- [9] Han J P, Xu G Y, Ding B, Pan J, Dou H and MacFarlane D R 2014 *J. Mater. Chem. A* **2** 5352–7
- [10] Jinghuang L *et al* 2018 *Adv. Sci.* **5** 1700687
- [11] Jinghuang L *et al* 2017 *J. Mater. Chem. A* **5** 24594–601
- [12] Jinghuang L *et al* 2017 *J. Power Sources* **362** 64–72
- [13] Wang Y Q, Wang G Z, Wang H Q, Liang C H, Cai W P and Zhang L D 2010 *Chem. Eur. J.* **16** 3497–503
- [14] Luo D B, Wu L Z and Zhi J F 2009 *ACS Nano* **3** 2121–8
- [15] Wang Q, Subramanian P, Li M S, Yeap W S, Haenen K, Coffinier Y, Boukherroub R and Szunerits S 2013 *Electrochem. Commun.* **34** 286–90
- [16] Honda K, Rao T N, Tryk D A, Fujishima A, Watanabe M, Yasui K and Masuda H 2001 *J. Electrochem. Soc.* **148** A668–79
- [17] Wang X J, Feng J, Bai Y C, Zhang Q and Yin Y D 2016 *Chem. Rev.* **116** 10983–1060
- [18] Caruso F, Shi X Y, Caruso R A and Susha A 2001 *Adv. Mater.* **13** 740–4
- [19] Wang Z Y, Zhou L and Lou X W 2012 *Adv. Mater.* **24** 1903–11
- [20] Yin Y D, Rioux R M, Erdonmez C K, Hughes S, Somorjai G A and Alivisatos A P 2004 *Science* **304** 711–4
- [21] Fan H J, Gosele U and Zacharias M 2007 *Small* **3** 1660–71
- [22] Petrak V *et al* 2017 *Carbon* **114** 457–64
- [23] Kondo T, Lee S, Honda K and Kawai T 2009 *Electrochem. Commun.* **11** 1688–91
- [24] Patrick E, Orazem M E, Sanchez J C and Nishida T 2011 *J. Neurosci. Methods* **198** 158–71
- [25] Motoki T, Gao W, Kiyono S and Ono T 2006 *Meas. Sci. Technol.* **17** 495–9
- [26] Kim J H, Lee S K, Kwon O M and Lim D S 2009 *J. Nanosci. Nanotechnol.* **9** 4121–7
- [27] Lee S K, Kim J H, Jeong M G, Song M J and Lim D S 2010 *Nanotechnology* **21** 505302
- [28] Thangala J, Vaddiraju S, Bogale R, Thurman R, Powers T, Deb B and Sunkara M K 2007 *Small* **3** 890–6
- [29] Frey G L, Rothschild A, Sloan J, Rosentsveig R, Popovitz-Biro R and Tenne R 2001 *J. Solid State Chem.* **162** 300–14
- [30] Boulova M, Rosman N, Bouvier P and Lucazeau G 2002 *J. Phys.: Condens. Matter* **14** 5849–63
- [31] Shigesato Y, Murayama A, Kamimori T and Matsuhira K 1988 *Appl. Surf. Sci.* **33–34** 804–11
- [32] Wang X P, Yang B Q, Zhang H X and Feng P X 2007 *Nanoscale Res. Lett.* **2** 405–9
- [33] Takase A and Miyakawa K 1991 *Japan. J. Appl. Phys.* **30** L1508–11
- [34] Pfeiffer R, Kuzmany H, Knoll P, Bokova S, Salk N and Gunther B 2003 *Diam. Relat. Mater.* **12** 268–71
- [35] Hees J, Heidrich N, Pletschen W, Sah R E, Wolfer M, Williams O A, Lebedev V, Nebel C E and Ambacher O 2013 *Nanotechnology* **24** 025601
- [36] Ashcheulov P *et al* 2013 *Eur. Phys. J. B* **86** 443
- [37] Williams O A and Nesladek M 2006 *Phys. Status Solidi a* **203** 3375–86
- [38] Ferrari A C and Robertson J 2001 *Phys. Rev. B* **63** 121405(R)
- [39] Zhu T, Chong M N and Chan E S 2014 *ChemSusChem* **7** 2974–97
- [40] Kelsey G S 1977 *J. Electrochem. Soc.* **124** 814–9
- [41] Anik M and Osseo-Asare K 2002 *J. Electrochem. Soc.* **149** B224–33
- [42] Johnson J W and Wu C L 1971 *J. Electrochem. Soc.* **118** 1909–12
- [43] Kulesza P J and Faulkner L R 1988 *J. Am. Chem. Soc.* **110** 4905–13
- [44] Lee S K, Song M J, Kim J H, Kan T S, Lim Y K, Ahn J P and Lim D S 2014 *NPG Asia Mater.* **6** e115
- [45] Chen Z W, Xu L B, Li W Z, Waje M and Yan Y S 2006 *Nanotechnology* **17** 5254–9
- [46] Nkosi D, Pillay J, Ozoemena K I, Nouneh K and Oyama M 2010 *Phys. Chem. Chem. Phys.* **12** 604–13
- [47] Anson F C 1966 *Anal. Chem.* **38** 54–7
- [48] Adams R N 1969 *Electrochemistry at Solid Electrodes* (New York: Dekker)